Single-molecule imaging of cytoplasmic dynein reveals the mechanism of motor activation and cargo capture

Nireekshit Addanki Tirumala[1] **and Vaishnavi Ananthanarayanan**[1,2,✉]

[1]Centre for BioSystems Science and Engineering, Indian Institute of Science, Bangalore, India
[2]Current affiliation: EMBL Australia Node in Single Molecule Science, School of Medical Sciences, University of New South Wales, Australia

Cytoplasmic dynein 1 (dynein) is the primary minus end-directed motor protein in most eukaryotic cells (1). Dynein remains in an inactive conformation until the formation of a tripartite complex comprising dynein, its regulator dynactin and a cargo adaptor (2–5). Thereupon, dynein transports cargo towards the minus ends of microtubules. How this process of motor activation occurs is unclear, since it entails the formation of a three-protein complex inside the crowded environs of a cell. Here, we employed live-cell, single-molecule imaging to visualise and track fluorescently tagged dynein. First, we observed that dynein that bound to the microtubule engaged in minus end-directed movement only ~30% of the time and resided on the microtubule for a short duration. Next, using high-resolution imaging in live and fixed cells, we discovered that dynactin remained persistently attached to microtubules, and endosomal cargo remained in proximity to the microtubules and dynactin. Finally, we employed two-colour imaging to visualise cargo movement effected by single motor binding. Taken together, we discovered a search strategy that is facilitated by dynein's frequent microtubule binding-unbinding kinetics: (1) in a futile event when dynein does not encounter cargo anchored in proximity to the microtubule, dynein unbinds and diffuses into the cytoplasm, (2) when dynein encounters cargo and dynactin upon microtubule-binding, it moves cargo in a short run. In conclusion, we demonstrate that dynein activation and cargo capture are coupled in a step that relies on reduction of dimensionality to enable minus end-directed transport *in vivo*.

cytoplasmic dynein | dynactin | cargo trafficking | single-molecule imaging
Correspondence: ***vaish@unsw.edu.au***

Results and Discussion

Dynein interacts transiently with the microtubule

To visualise the behaviour of dynein in HeLa cells expressing mouse DYNH1C1-GFP (mDHC-GFP, (6)), we adapted and optimised highly inclined and laminated optical sheet (HILO) microscopy ((7), Extended Data Fig. 1a). When cells expressing low levels of mDHC-GFP were observed under a spinning disk confocal (SD) microscope, the fluorescence signal appeared cytosolic, with no discernible dynein punctae (Extended Data Fig. 1b). However, when the same cells were observed using our modified HILO microscopy, distinct fluorescent spots were visible.

We adapted our microscopy protocol to obscure dynein diffusing in the cytoplasm and to only observe dynein that bound to and resided on the microtubule ((8, 9), MT, Fig. 1a, see Methods). We observed that dynein spots appeared afresh and remained in the field of imaging for a short duration (Fig. 1b, Supplementary Video 1). We intuited that these intensity traces corresponded to events where single dynein molecules previously diffusing in the cytoplasm bound to MTs (Extended Data Fig. 1c-e).

To confirm that the appearance of fluorescent signal on the MT corresponded to binding of a single molecule of dynein to the MT, we analysed the intensity of these fluorescent spots (Fig.1c). For single dynein molecules, we would expect the intensity histogram to fit to a sum of two Gaussian distributions, one corresponding to a GFP fluorescing from one DHC and the other corresponding to two GFPs fluorescing from both DHCs in the genetic background of these cells. The former primarily arose due to photobleaching of GFP during the course of imaging. Accordingly, the intensity histogram of these fluorescent spots revealed that we indeed observed single dynein molecules since the intensity histogram fit best to a sum of 2 Gaussians, with the mean of the first being half that of the second (Fig. 1c).

Next, we analysed the x, y vs t tracks of single molecules of dynein that bound afresh from the cytoplasm to the MT (Fig. 1d). Based on automated thresholding (see Methods), we classified the tracks as stationary, minus end-directed and plus end-directed. The plus ends of the MT were predominantly at the periphery in these elongated cells (Extended Data Fig. 1f), and hence we annotated movement towards the cell center as minus end-directed, and movement away, plus end-directed. We observed that ~50% of all the dynein molecules tracked (n=177/329, N=3 independent experiments from >50 cells) remained stationary upon MT binding, while ~30% (n=95/329) moved towards the minus end (Fig. 1e). The remaining ~20% moved towards the plus end and arose likely due to attachment of dynein to cargo being moved to the plus end by kinesins (Fig. 1e). The velocity measured for minus-end directed movement of single dyneins was 1.2 ± 0.7 μm/s (mean ± s.d.), similar to values reported for mammalian dynein previously (10, 11). We also confirmed that the underlying MT was stable, did not undergo sliding, and therefore did not contribute to the dynein behaviour we observed (Extended Data Fig. 1g).

We then measured the mean residence time of dynein on the MTs to be ~0.55s (95% confidence interval (CI): 0.51-0.59s) (Fig. 1f). We verified that this short residence time of

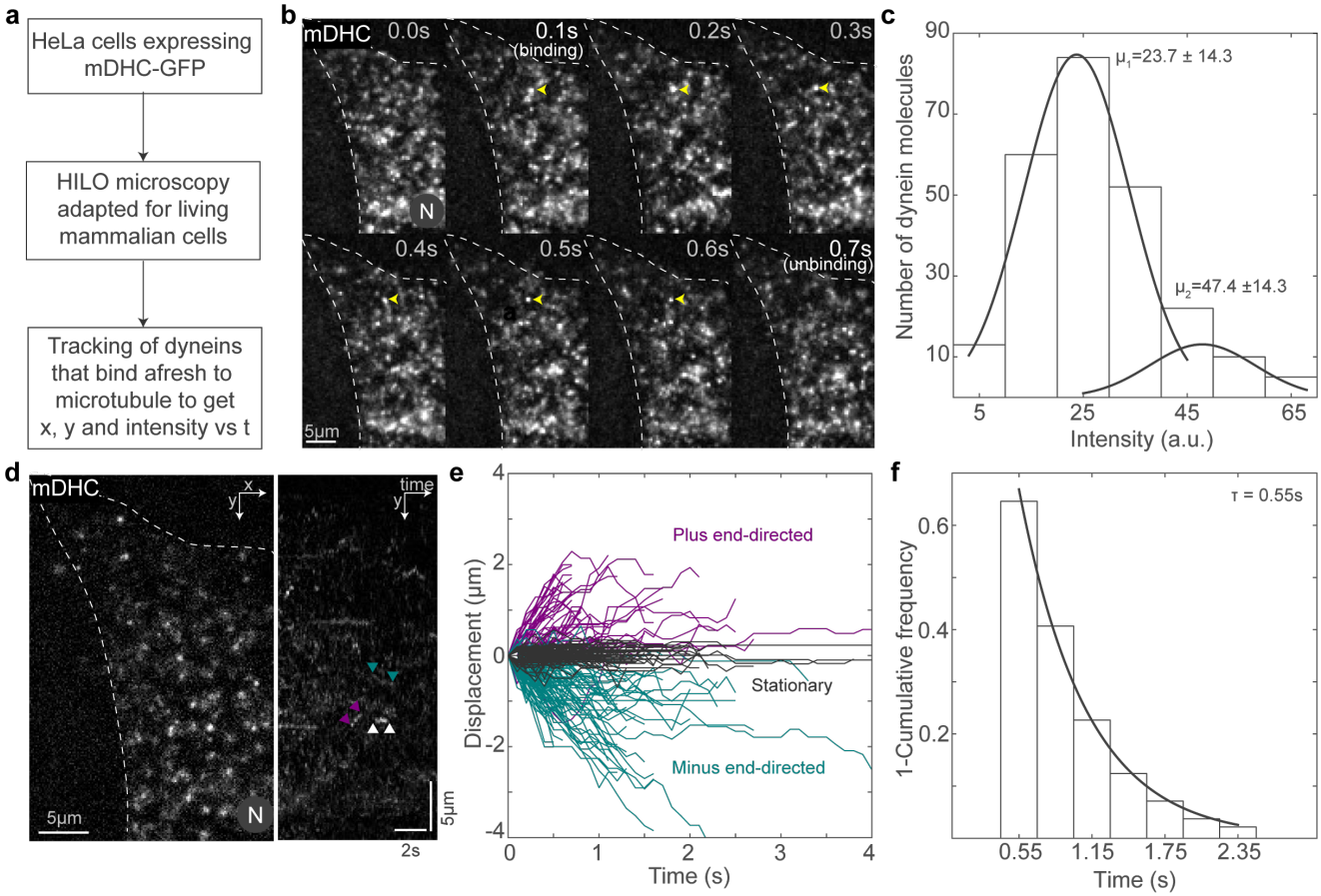

Fig. 1. Visualisation of single molecules of dynein in living cells. **a**, Schematic of the protocol followed for the visualisation of single molecules of dynein. **b**, Montage of HILO images showing representative binding and unbinding events of a single fluorescent mDHC molecule ('(binding)' and '(unbinding)'). The single molecule is indicated with yellow arrowheads for the duration of the time it remains bound in the field of view. Time is indicated at the top right of each image in the montage. **c**, Intensity histogram of single molecules of dynein with the Gaussian fits (grey line). The mean ± s.d. of the Gaussian distributions is indicated above the fits. **d**, HILO image (left) and kymograph (right) of a cell expressing mDHC-GFP. Representative stationary, minus end-directed and plus end-directed events are indicated with the white, teal and magenta arrowheads respectively in the kymograph. **e**, Plot of displacement vs. time for the single-molecule events tracked, showing stationary events (grey), minus end-directed events (teal) and plus end-directed events (magenta). **f**, Histogram with the residence time of dynein on the MT on the x axis and 1-cumulative frequency on the y axis. The exponential fit (grey line) gave a mean residence time ('τ') of ~0.55 s. In **b** and **d**, 'N' marks the location/direction of the nucleus.

dynein on MTs was a true representation of the duration of time dynein remained attached to the MT and not convolved by GFP's photobleaching time (Extended Data Fig. 1h and i). Further, by knocking down endogenous HeLa DYNC1H1 (hDHC), we verified that our observations were not an artefact of expression of mDHC-GFP in this background (Extended Data Fig. 2 a-h). To the best of our knowledge, these are the first observations of single molecules of dynein in mammalian cells and indicate that dynein likely exists in an inactive state inside the cell, similar to reports from *in vitro* studies (2–5).

Dynactin remains persistently associated with MTs

Next, we aimed to visualise the dynamics of the second player in the tripartite complex, dynactin. Dynactin was first identified as a complex that was required for dynein-driven motility of vesicles *in vitro* (12). Several recent pieces of research have identified dynactin as an essential part of the active dynein complex (13–15). Dynactin is a multi-subunit complex which binds to MTs independently of dynein via its N-terminal p150 subunit (16). However, dynactin's interaction with dynein has been observed to be improbable in the absence of the cargo adaptor (2–5).

The +TIP protein EB1 has been found to recruit another +TIP protein, CLIP-170, which in turn binds and clusters dynactin via its p150 subunit at growing MT plus ends (17). MT plus ends decorated with dynactin also accumulated dynein at these sites, and evidence suggested that cargo transport was initiated when these MT plus ends contacted intracellular cargo (18, 19). However, MT plus end-mediated initiation of dynein-driven transport appears to vary with cell type and context (17, 20, 21). Therefore, using SD microscopy in combination with super-resolution radial fluctuations (SRRF, (22)) we first quantified the localisation of p150 (Fig. 2a). Our high-resolution images revealed that only ~17% of the MT plus ends were enriched with p150, and p150 appeared bound along the entire length of the MT lattice (Fig. 2b). Further, by quantifying the intensities of mDHC-GFP expressed in our cells, we concluded that the significant MT plus end localisation of dynein reported in earlier studies (2, 23) might have been an artefact of dynein overexpression (Extended Data Fig. 3a, b).

However, the dynactin complex has been observed to show

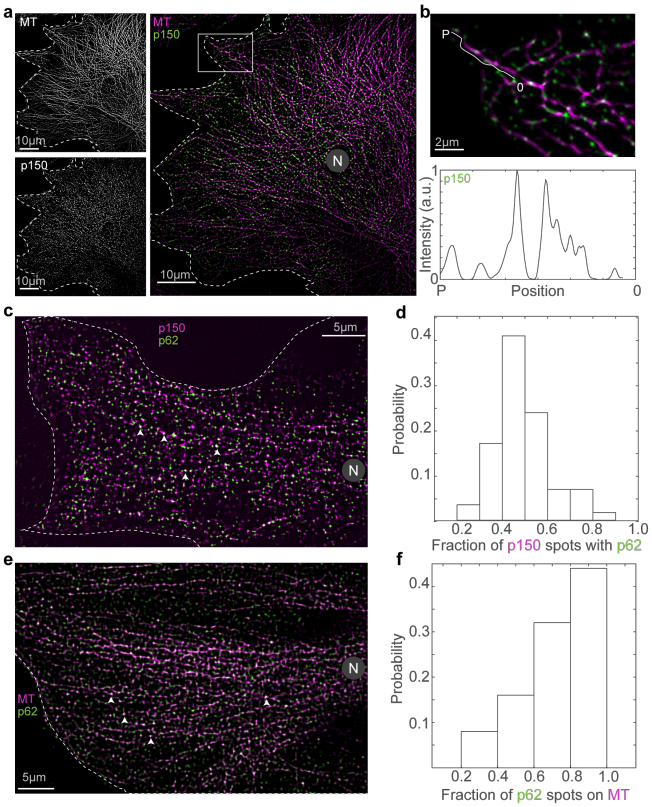

Fig. 2. The dynactin complex binds along the entire length of the MT. a, Immunofluorescence images of MT (top left), p150 (bottom left) and their merge (right) obtained using SD microscopy + SRRF. **b**, Enlarged view of the area marked with the white rectangle in a (top) and the line profile of p150 intensity along the length of a representative MT from the plus end ('P') to ~6 µm from the plus end of the MT ('0'). **c**, Immunofluorescence images of p62 (green) and p150 (magenta) obtained using SD microscopy + SRRF. The white arrowheads indicate representative p150 spots that also contain p62. **d**, Histogram of the probability of cooccurrence of p62 with p150, indicating a high likelihood of presence of the entire complex at a p150 spot. **e**, Immunofluorescence images of MT (magenta) and p62 (green) obtained using SD microscopy + SRRF. The white arrowheads indicate representative p62 spots that occur on the MT. **f**, Histogram of the probability of cooccurrence of p62 on the MT, which points to a high likelihood for the presence of the entire dynactin complex on the MT. In **a**, **b**, **c** and **e**, 'N' marks the location/direction of the nucleus.

no MT-binding in the absence of dynein in *in vitro* assays (3). To ascertain that the p150 spots that we observed in these cells represented the entire dynactin complex, we used SRRF to visualise p150 in concert with another dynactin subunit, p62 (Fig. 2c). The p62 subunit of dynactin is located in the pointed end complex of dynactin (16), and colocalisation of p62 with p150 would indicate the presence of the complete dynactin complex. We observed that 49 ± 12% (mean ± s.d.) of the p150 spots colocalised with p62 (n=21,934/44,306 spots from N=2 independent experiments with 59 cells, Fig. 2d). So too, we used SRRF to additionally visualise the localisation of p62 on MTs. The presence of p62 on MTs would indicate association with the MT of a subunit which does not normally do so unless it is part of the entire dynactin complex. Therefore, occurrence of p62 on the MT would imply localisation of the entire complex on the MT via p150. We observed that 74 ± 18% (mean ± s.d.) of the p62 spots (n=59,715/79,639 spots from 1 experiment with 25 cells) were present on MTs (Fig. 2e, f). Therefore, the complete dynactin complex is likely present along the length of the MT lattice. Additionally, fluorescently tagged p150 had residence times on the MT that far exceeded that of dynein, with most spots of p150 remaining bound to the MT for the entire duration of the time-lapse video (~30 s) (Extended Data Fig. 3c, Supplementary Video 2). Further, we observed that depletion of p150 through siRNA mediated silencing reduced the levels of both p150 and p62 along the MT lattice (Extended Data Fig. 3d-i) To test that the perturbation of dynactin localisation along the MT lattice resulted in reduced dynein activity, we depleted p150 using siRNA mediated silencing. As expected, we observed a reduction in the proportion of dynein molecules that moved towards the MT minus ends with a concomitant increase in the proportion that moved towards the plus ends (Extended Data Fig. 4 a-d).

Endosomes remain close to MTs and move in short bursts

We then sought to understand how dynein interacted with the third component of the active complex - the cargo adaptors. The endosomal cargo adaptors, Hook proteins, have been observed to remain persistently bound to their respective cargo (24, 25). Therefore, we used endosomal cargo as a proxy for the cargo adaptor. To avoid artefacts from overexpressing fluorescently tagged Rab5 to visualise early endosomes (26), we employed cells that had taken up 10kDa dextran conjugated with Alexa 647 via fluid-phase endocytosis (Extended Data Fig. 5a).

Following a short pulse and chase, we observed Rab5-positive fluorescent compartments (Extended Data Fig. 5b, Supplementary Video 3). We visualised dextran vesicles in 10s-timelapses and observed that ~85% of them were immobile (Fig. 3a, Supplementary Video 4), with only ~15% of these vesicles moving >1 µm during this time (Fig. 3b). Strikingly, the dextran vesicles displayed uninterrupted minus end-directed runs that lasted only 0.56 ± 0.25 s (mean ± s.d.) on an average (Fig. 3c) (n=719 dextran vesicles from N=1 independent experiment with > 30 cells). These results are comparable to the run-and-pause behavior observed for endosomal cargo in previous studies (10, 11).

Next, we probed the localisation of the dextran vesicles with respect to the MT. First, we imaged dextran vesicles and MTs in live cells and observed that the vesicles were in proximity to the MTs (Fig. 3d). We also observed that the dextran vesicles remained close to MTs even while they had no apparent tether to the MTs via motor proteins, and therefore stationary (Supplementary Video 5) in minute-long live cell time-lapse images. Then, to understand if the dextran vesicles could diffuse away from their original locations on the MT upon motor unbinding, we depolymerised MTs using nocodazole and visualised movement of the vesicles thereafter (Extended Data Fig. 5c, Supplementary Video 6). Confirming previous findings (10, 11), we measured a lower diffusion coefficient for the vesicles in the absence of MTs (Extended Data Fig. 5d), likely implicating high intracellular crowding in constraining vesicle diffusion (11). Finally, we used SRRF to visualise Rab5 in concert with p62 in living cells, and observed that ~70% of the Rab5 spots colocalised with p62 (n=8,795/12,848 vesicles from N=2 independent experiments with >20 cells each), indicating that cargo and dynactin are

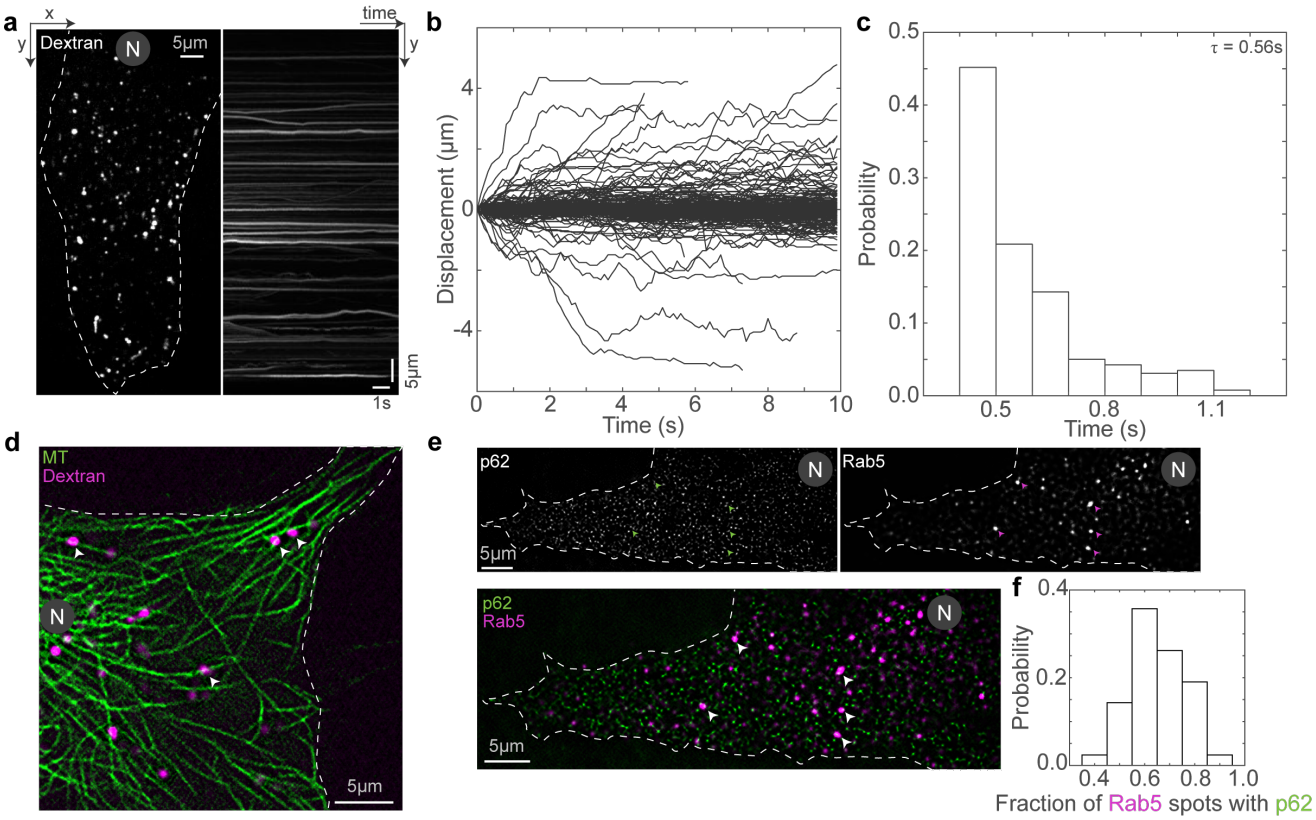

Fig. 3. Most dextran vesicles are stationary at a given time. **a**, SD microscopy image from a time-lapse of dextran vesicles in HeLa cells (left) and the corresponding kymograph (right). **b**, Plot of displacement vs. time of dextran vesicles in HeLa cells. **c**, Histogram with the duration of minus end-directed run on the x axis and probability on the y axis. **d**, SD + SRRF image of MTs (green) and dextran vesicles (magenta) in live cells. The white arrowheads indicate representative vesicles on the MT. **e**, SD + SRRF image of p62 (top left), dextran vesicles (top right) in live cells and their merge (bottom, p62 in green and dextran in magenta). The white arrowheads in the merged image indicate representative vesicles that colocalise with p62, and are shown as green and magenta arrowheads in the p62 and dextran images respectively. **f**, Histogram of the probability of cooccurrence of p62 with Rab5, indicating a high likelihood of dynactin being present in a complex with endosomal cargo. In **a**, **d** and **e**, 'N' marks the location/direction of the nucleus.

in proximity to each other on the MT (Fig. 3e, f).

Dynein molecules are activated upon attachment to dynactin and cargo on the MT Thus far, we discovered that while dynein transiently interacted with the MT, dynactin and cargo appeared together and close to MTs. We therefore sought to understand how dynein interacted with the dynactin-cargo complexes on MTs. First, we performed dual-colour imaging of dynein and dextran and observed that vesicles that had dynein signal were more likely to move towards the minus end of MTs as expected (Extended Data Fig. 5e-g). Next, by comparing the intensity of dynein on dextran vesicles to single molecule binding events, we estimated that, on an average, there were 1-2 dynein molecules bound to a dextran vesicle (Extended Data Fig. 5h).

Finally, to verify if single molecules of dynein could be activated and perform minus end-directed movement when they stochastically bound to MTs and encountered dynactin-cargo complexes, we performed fast dual-colour HILO imaging of single dynein molecules and dextran vesicles. To rule out artefacts due to the presence of both untagged hDHC and mDHC in these cells, we performed these experiments in cells where we depleted hDHC. In these videos (Supplementary Video 7), we observed instances where previously stationary dextran vesicles started moving together with mDHC-GFP towards the MT minus ends upon dynein binding (Fig. 4a-d, n=8/9 events from N=2 independent experiments with ~100 cells).

Conclusions

Taken together, we observed that: (i) single molecules of dynein stochastically interacted with MTs. (ii) In some instances, this attachment to MTs resulted in a successful encounter with the dynactin-cargo complex and therefore, a minus end-directed run that lasted about half a second. (iii) Dynein detached from the cargo to conclude the run (Fig. 4e). For long-range movement of endosomal cargo, these steps are required to be repeated multiple times. Such strategies have been described in the past for transcription factors seeking specific sequences along the DNA (27, 28). Since cytoplasmic dynein is the only minus end directed motor in many cell types, how dynein interacts with and transports different types of cargo is an interesting question. Recent research suggests that cargo specific adaptors like BicD2 (for Rab6-positive cargo), Hook1/3 (for Rab5-positive cargo) have differential interaction with dynein (3). These cargo adaptors could modulate the interaction time of dynein

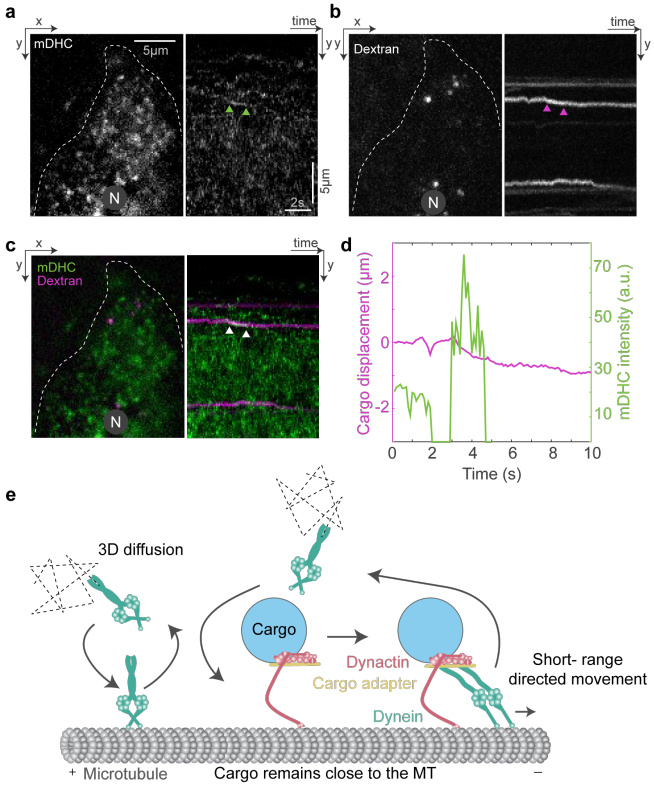

Fig. 4. Cargo capture and dynein activation are coupled a, Image of dynein (left), from a HILO microscopy time-lapse video and the corresponding kymograph (right). A representative binding event of a single dynein (green arrowheads) is shown in the kymograph. **b**, Image of dextran (left) from the same HILO microscopy time-lapse video from which **a** was obtained and the corresponding kymograph (right). A representative minus end directed run of the dextran vesicle (magenta arrowheads) is shown in the kymograph. **c**, Merge of images (left) shown in **a**, **b** and the corresponding kymograph (right). The white arrow heads point to dynein and dextran moving together towards the minus end. **d**, Plot of displacement vs time of the dextran vesicle (magenta) indicated in **a**, alongside the intensity of dynein on that vesicle (green), showing a short minus-end directed run of the vesicle upon dynein-binding. **e**, Schematic of dynein's cargo search strategy. In **a**, **b** and **c**, 'N' marks the location/direction of the nucleus.

molecules with the cargo thereby leading to different trajectories. Such stochastic binding and unbinding allow the same dynein molecule to sample and interact with a wide range of cargo, akin to round robin scheduling. Movement to the plus or minus ends of MTs could therefore also be tuned by slightly increasing the bias in one direction, for example by increasing the number of adaptors for dynein on a cargo destined towards the minus end.

Methods

Cell culture. HeLa cells were cultured in Dulbecco's Modified Eagle Media (DMEM) containing 100 units/mL Penicillin, 0.1 mg/mL Streptomycin, 2 mM L-Glutamine, 400 μg/mL Geneticin (HiMedia Laboratories) and supplemented with 10% fetal bovine serum (Sigma Aldrich). Cells were grown in an incubator at 37°C under 5% CO_2. During live-cell imaging, cells were maintained in live-cell imaging solution (140 mM NaCl, 2.5 mM KCl, 1.8 mM CaCl2, 1 mM MgCl2, 4 mg/mL D-Glucose, 20 mM HEPES) at 37°C using a stage-top incubator (Oko Labs).

RNAi experiments. For all RNAi experiments, cells were first grown in glass-bottom imaging dishes (Cat. no. 81518, Ibidi) for 48 h, transfected with the appropriate concentration of siRNA using Jet Prime transfection reagent (Cat. no. 114, Polyplus) and imaged after 48 h. For hDHC RNAi the following siRNA sequence was used: 5'-ACA-UCA-ACA-UAG-ACA-UUC-A-3'10. For p150 RNAi the following siRNA sequences were used: 5'-GUA-CUU-CAC-UUG-UGA-UGA-A-3', 5'-GAU-CGA-GAG-ACA-GUU-AUU-A-3' (17). siRNA oligonucleotides were procured from Eurogentec, Belgium. To quantify the knockdown of proteins, the cells were lysed 48 hours after siRNA transfection to obtain protein solution and SDS-PAGE, western blotting was performed. The following primary antibodies were used to visualise proteins of interest and controls: Rabbit DYNC1H1 Polyclonal Antibody (PA5-49451, Invitrogen, 0.5 μg/mL), Rabbit Dynactin 1 Polyclonal Antibody (PA5-37360, Invitrogen, 0.5 μg/mL), Mouse GAPDH Loading Control Antibody (MA5-15738, Invitrogen, 0.5 μg/mL), Rabbit Actin Polyclonal Antibody (ab8227, AbCam, 0.5 μg/mL). The following secondary antibodies were used: Anti-Rabbit HRP (31460, Invitrogen, 0.16 μg/mL) and Anti-Mouse HRP (62-6520, Invitrogen, 0.3 μg/mL).

Immunofluorescence. To immunostain p150 and tubulin, cells were first grown for 48 h in glass-bottom imaging dishes (Cat. no. 81518, Ibidi) and fixed in ice-cold methanol at -20°C for 3 min. Cells were washed thrice in phosphate buffered saline (PBS) for 5 min each and incubated in blocking buffer (5% BSA in PBS) for 60 min. Subsequently, the cells were incubated with p150 and α-tubulin antibodies in antibody dilution buffer (1% BSA in PBS) for 60 min. Cells were then washed thrice in PBS for 5 mins and incubated with secondary antibodies in antibody dilution buffer for 45 min. At the end of incubation with secondary antibodies, the cells were washed with PBS and imaged immediately. The following primary antibodies were used. Rabbit Dynactin 1 Polyclonal Antibody (PA5-21289, Invitrogen, 2 μg/mL), Mouse α Tubulin Monoclonal Antibody (32-2500, Invitrogen, 2 μg/mL). The secondary antibodies used were Donkey Anti-Rabbit A555 Antibody (A31572, Invitrogen, 0.4 μg/mL) and Goat Anti-Mouse A647 Antibody (A28181, Invitrogen. 2 μg/mL)

To immunostain p150 and p62, p62 and α-Tubulin and EB1 and α-Tubulin the following method was used. Cells were first grown for 48 h in glass bottomed imaging dishes and fixed in ice-cold methanol at -20°C for 3 min. Subsequently, the cells were washed thrice in PBS for 5 min each and incubated in antibody dilution buffer (2% BSA, 0.1% Triton-X100, in PBS) for 10 min. Next, the cells were incubated in antibody dilution buffer containing the appropriate antibodies for 60 mins. Cells were washed thrice in PBS for 5 min each and incubated with appropriate secondary antibodies in antibody dilution buffer for 30 min. At the end of incubation with secondary antibodies, the cells were washed well in PBS and imaged immediately. The following primary antibodies were used. Rabbit Dynactin 1 Polyclonal Antibody (PA5-

21289, Invitrogen, 2.5 µg/mL), Rabbit Alpha Tubulin Monoclonal Antibody (PA5-22060, Invitrogen, 2 µg/mL), Mouse Dynactin 4 Monoclonal Antibody (MA5-17065, Invitrogen, 2 µg/mL) and Mouse EB1 Monoclonal Antibody (412100, Invitrogen, 2 µg/mL). The secondary antibodies used were Donkey Anti-Rabbit A647 Antibody (A32795, Invitrogen, 2 µg/mL) and Goat Anti-Mouse A555 Antibody (A21422, Invitrogen. 2 µg/mL).

To immunostain Rab5 and p62, cells were first fixed in 4% Paraformaldehyde (PFA) for 15 mins. The cells were washed well in PBS and incubated for 45 min in antibody staining solution (0.2% Saponin, 0.1% BSA and 0.02% Sodium Azide in PBS) containing primary antibodies against Rab5 and p62. Subsequently, cells were washed well in PBS and incubated for 45 min in antibody staining solution containing appropriate secondary antibodies. Cells were washed well in PBS and imaged immediately. The following primary antibodies were used. Rabbit Rab5 Monoclonal Antibody (3547, Cell Signaling Technology, 14 µg/mL), Mouse Dynactin 4 Monoclonal Antibody (MA5-17065, Invitrogen, 2 µg/mL). The secondary antibodies used were Donkey Anti-Rabbit A647 Antibody (A32795, Invitrogen, 2 µg/mL) and Goat Anti-Mouse A555 Antibody (A21422, Invitrogen. 2 µg/mL).

Dextran uptake. To visualise fluorescent dextran vesicles HeLa cells that were grown in glass-bottom imaging dishes (Cat. no. 81518, Ibidi) for 48 h were transferred to serum-free DMEM for 4 h in a 37°C CO_2 incubator. Subsequently, the cells were pulsed for 10 min in complete DMEM containing 200 µg/mL A647-Dextran (D-22914, Invitrogen). Cells were then washed well with live-cell imaging solution before proceeding for microscopy. In all experiments, imaging was completed within 45 min of dextran uptake.

Transfection. To visualise fluorescently tagged proteins, cells were transfected with the appropriate plasmids using Jet Prime Transfection Reagent (Cat. no. 114, Polyplus). 3 h after transfection, the cells were washed well in PBS, grown in complete DMEM at 37°C and imaged ~20 h later. The following plasmids were used in this study. (i) mCherry-tubulin was a gift from Mariola Chacon, TUD, Dresden. (ii) Gal4T-mCherry was a gift from Thomas Pucadyil, IISER Pune. (iii) mCherry-DCTN1 was a gift from Prof. Kozo Tanaka, Tohoku university, Japan. (iv) mCherry-Rab5 was a gift from Gia Voeltz (Addgene plasmid - 49201).

Microscopy. All imaging was performed on a Nikon Ti2E inverted microscope equipped with a Toptica MLE laser combiner, Nikon H-TIRF Module, Yokogawa CSU-X1 spinning disk module, an Andor iXon 897 EMCCD camera and an Oko Lab stage top incubator. The microscope was controlled using Nikon NIS Elements software or Micromanager (29).

HILO microscopy and particle tracking. For HILO microscopy, a Nikon 100X 1.49NA TIRF objective was used. We optimised the HILO microscopy setting for each cell: First, to avoid overexpression artefacts, we visualised cells expressing low levels of mDHC-GFP. The diameter of the illuminated area was kept constant at 30 µm and the long axis of cell was aligned perpendicular to the excitation laser. Finally, we adjusted the angle of incidence of the excitation laser, such that the fluorescent spots in a plane ~0.5 µm from the cover slip appeared bright and distinct. The incidence angle and orientation of excitation laser beam were adjusted using the H-TIRF module and the laser power (50 mW at fiber) was kept at 40%. To visualise single molecules of dynein, time-lapse images were acquired at 50 fps with 20 ms exposure per frame.

To improve the signal-to-noise ratio, a five-frame sliding average of the time-lapse images was used for particle tracking. In these videos, the appearance and subsequent disappearance of intensity at a particular location was classified as a binding event. Such binding events were visually identified and tracked from the start to end frame using Low Light Tracking tool (30) in Fiji/ImageJ (31). The fluorescent spots were classified as stationary, minus-end moving or plus-end moving by marking a region close to the nucleus as the minus end and calculating the displacement of fluorescent spots with respect to the minus end. Particles moving away from the nucleus for >0.32 µm were classified as plus-end moving, and particles with displacement >0.32 µm towards the nucleus were minus-end directed, and particles with net displacement <0.32 µm were classified as stationary.

For dual channel imaging of dynein and dextran, videos were acquired at 20 fps with 25 ms exposure per channel. To observe dynein-dextran interaction with a better signal-to-noise ratio, a two-frame sliding average of time-lapse images was used.

Spinning disk (SD) confocal microscopy and image analysis. To quantify the correlation between expression level of dynein and its clustering, z-stack images of live HeLa cells expressing mDHC-GFP were acquired using a 60x, 1.4 NA objective with 50 ms exposure. The intensity comparison was done for the lowest plane at which clusters were distinctly visible. The dynamics of mCherry-p150 in cells were visualised by acquiring 60-s long movies of the cell with a 1.4 NA 60x objective, 100 ms exposure per frame and 1 s interval between frames. The dynamics of dextran vesicles along the MTs was visualised by acquiring 30-s long movies of the cell with a 60x, 1.4 NA objective, 100 ms sequential exposure/channel and 1 s interval between frames. The dynamics of dextran vesicles was visualised by acquiring a 10-s long movie with 100x 1.49NA TIRF objective, 100 ms exposure/frame and no interval between frames. The movement of dextran vesicles was classified in the following way: the movement between two consecutive frames was classified as zero if it was less than 50 nm (the tracking accuracy of low light tracking tool under the imaging conditions used30). Then, displacement for four consecutive frames towards or away from the nucleus was classified as a minus or plus end-directed run.

The SD+SRRF images were obtained by taking the mean of the radiality map of 100 images of a single field acquired

under a 100x, 1.49NA objective with the SD confocal microscopy setup. The radiality magnification in SRRF was set to 4 for all experiments. To visualise the association between MTs and dextran vesicles in live cells, the SRRF acquisition settings used were 20ms exposure, ring radius of 0.5 for MTs and 3 for dextran. To visualise p62 with tubulin and EB1 with tubulin, 20 ms exposure and ring radius of 0.5 was used. To visualise p150 with tubulin, and p150 with p62 the SRRF acquisition settings used were 100 ms exposure, ring radius of 1. Finally, to visualise p62 with Rab5, 20ms exposure was used in both channels. A ring radius of 0.5 and 3 were used for p62 and Rab5, respectively.

The cooccurrence of p150 with p62 was quantified by first thresholding SRRF images of p150 for the top 5% of intensity. The number of p150 spots was counted N_{p150}, and a mask was created. Then, the SRRF image of p62 in the same cells was combined with the p150 mask using AND operation in Fiji. The resultant image was thresholded and the number of spots counted (N_{p62}). N_{p62}/N_{p150}*100 gave the percentage of p150 spots with p62. A similar procedure was used to quantify the percentage of p62 spots that occurred on the MT and also the percentage of Rab5 spots that were associated with p62.

To quantify the effect of p150 knock-down on the levels of p150, p62 along the MT, ROIs were drawn along distinct MT segments that were randomly chosen in SRRF images of MT, and the mean intensities of p150 or p62 in these ROIs were measured.

Curve fitting and data visualisation. For the intensity fits in Fig. 1c, the intensity values of tracked dynein molecules was plotted as a histogram. This distribution was fit by a sum of two Gaussians with the same standard deviation (σ). The smaller mean was constrained between 15-30 and the larger mean was constrained between 35-50. For the exponential fit in Fig. 1f, the probability vs residence time histogram of dynein on the MTs was obtained from the lengths of all single molecule binding events. From this distribution of 1-cumulative frequency of the residence time was obtained, and the time vs 1-cumulative frequency was fit to $\lambda.e^{-\lambda t}$ to obtain λ, the off-rate from MTs. The average residence time given by 1/λ.

All data was plotted using MATLAB (MathWorks). Figures panels were prepared using Adobe Illustrator.

ACKNOWLEDGEMENTS

We thank G Redpath and LA Chacko for constructive comments on the manuscript. VA is supported by EMBL Australia, and was supported by extramural funding from the Wellcome Trust/Department of Biotechnology–India Alliance (grant IA/18/1/503607), and the Women Excellence Award from the Science and Engineering Research Board, India, intramural funding from the Indian Institute of Science, and the RI Mazumdar Young Investigator Award and Department of Science and Technology (India) INSPIRE Faculty Award.

References

1. Victoria J. Allan. Cytoplasmic dynein. *Biochemical Society Transactions*, 39(5):1169–1178, oct 2011. ISSN 0300-5127. doi: 10.1042/BST0391169.
2. Daniël Splinter, David S. Razafsky, Max A. Schlager, Andrea Serra-Marques, Ilya Grigoriev, Jeroen Demmers, Nanda Keijzer, Kai Jiang, Ina Poser, Anthony A. Hyman, Casper C. Hoogenraad, Stephen J. King, and Anna Akhmanova. BICD2, dynactin, and LIS1 cooperate in regulating dynein recruitment to cellular structures. *Molecular Biology of the Cell*, 23(21): 4226–4241, nov 2012. ISSN 1059-1524. doi: 10.1091/mbc.e12-03-0210.
3. R. J. McKenney, W. Huynh, M. E. Tanenbaum, G. Bhabha, and R. D. Vale. Activation of cytoplasmic dynein motility by dynactin-cargo adapter complexes. *Science*, 345(6194): 337–341, jul 2014. ISSN 0036-8075. doi: 10.1126/science.1254198.
4. Max A Schlager, Ha Thi Hoang, Linas Urnavicius, Simon L Bullock, and Andrew P Carter. In vitro reconstitution of a highly processive recombinant human dynein complex. *The EMBO Journal*, 33(17):1855–1868, sep 2014. ISSN 0261-4189. doi: 10.15252/embj.201488792.
5. Kai Zhang, Helen E. Foster, Arnaud Rondelet, Samuel E. Lacey, Nadia Bahi-Buisson, Alexander W. Bird, and Andrew P. Carter. Cryo-EM Reveals How Human Cytoplasmic Dynein Is Auto-inhibited and Activated. *Cell*, 169(7):1303–1314.e18, jun 2017. ISSN 00928674. doi: 10.1016/j.cell.2017.05.025.
6. Ina Poser, Mihail Sarov, James R A Hutchins, Jean-Karim Hériché, Yusuke Toyoda, Andrei Pozniakovsky, Daniela Weigl, Anja Nitzsche, Björn Hegemann, Alexander W Bird, Laurence Pelletier, Ralf Kittler, Sujun Hua, Ronald Naumann, Martina Augsburg, Martina M Sykora, Helmut Hofemeister, Youming Zhang, Kim Nasmyth, Kevin P White, Steffen Dietzel, Karl Mechtler, Richard Durbin, A Francis Stewart, Jan-Michael Peters, Frank Buchholz, and Anthony A Hyman. BAC TransgeneOmics: a high-throughput method for exploration of protein function in mammals. *Nature Methods*, 5(5):409–415, may 2008. ISSN 1548-7091. doi: 10.1038/nmeth.1199.
7. Makio Tokunaga, Naoko Imamoto, and Kumiko Sakata-Sogawa. Highly inclined thin illumination enables clear single-molecule imaging in cells. *Nature Methods*, 5(2):159–161, feb 2008. ISSN 1548-7091. doi: 10.1038/nmeth1171.
8. Vaishnavi Ananthanarayanan, Martin Schattat, Sven K. Vogel, Alexander Krull, Nenad Pavin, and Iva M. Tolić-Nørrelykke. Dynein Motion Switches from Diffusive to Directed upon Cortical Anchoring. *Cell*, 153(7):1526–1536, jun 2013. ISSN 00928674. doi: 10.1016/j.cell.2013.05.020.
9. Vaishnavi Ananthanarayanan and Iva M. Tolić. Single-molecule imaging of cytoplasmic dynein in vivo. pages 1–12. 2015. doi: 10.1016/bs.mcb.2014.10.001.
10. Neftali Flores-Rodriguez, Salman S. Rogers, David A. Kenwright, Thomas A. Waigh, Philip G. Woodman, and Victoria J. Allan. Roles of Dynein and Dynactin in Early Endosome Dynamics Revealed Using Automated Tracking and Global Analysis. *PLoS ONE*, 6 (9):e24479, sep 2011. ISSN 1932-6203. doi: 10.1371/journal.pone.0024479.
11. Allison L. Zajac, Yale E. Goldman, Erika L.F. Holzbaur, and E. Michael Ostap. Local Cytoskeletal and Organelle Interactions Impact Molecular-Motor-Driven Early Endosomal Trafficking. *Current Biology*, 23(13):1173–1180, jul 2013. ISSN 09609822. doi: 10.1016/j.cub.2013.05.015.
12. S R Gill, T A Schroer, I Szilak, E R Steuer, M P Sheetz, and D W Cleveland. Dynactin, a conserved, ubiquitously expressed component of an activator of vesicle motility mediated by cytoplasmic dynein. *Journal of Cell Biology*, 115(6):1639–1650, dec 1991. ISSN 0021-9525. doi: 10.1083/jcb.115.6.1639.
13. Stephen J. King and Trina A. Schroer. Dynactin increases the processivity of the cytoplasmic dynein motor. *Nature Cell Biology*, 2(1):20–24, jan 2000. ISSN 1465-7392. doi: 10.1038/71338.
14. Saikat Chowdhury, Stephanie A. Ketcham, Trina A. Schroer, and Gabriel C. Lander. Structural organization of the dynein–dynactin complex bound to microtubules. *Nature Structural & Molecular Biology*, 22(4):345–347, apr 2015. ISSN 1545-9993. doi: 10.1038/nsmb.2996.
15. L. Urnavicius, K. Zhang, A. G. Diamant, C. Motz, M. A. Schlager, M. Yu, N. A. Patel, C. V. Robinson, and A. P. Carter. The structure of the dynactin complex and its interaction with dynein. *Science*, 347(6229):1441–1446, mar 2015. ISSN 0036-8075. doi: 10.1126/science.aaa4080.
16. Trina A. Schroer. DYNACTIN. *Annual Review of Cell and Developmental Biology*, 20(1): 759–779, nov 2004. ISSN 1081-0706. doi: 10.1146/annurev.cellbio.20.012103.094623.
17. Peter Watson and David J. Stephens. Microtubule plus-end loading of p150Glued is mediated by EB1 and CLIP-170 but is not required for intracellular membrane traffic in mammalian cells. *Journal of Cell Science*, 119(13):2758–2767, 2006. ISSN 00219533. doi: 10.1242/jcs.02999.
18. Patricia S. Vaughan, Pedro Miura, Matthew Henderson, Belinda Byrne, and Kevin T. Vaughan. A role for regulated binding of p150Glued to microtubule plus ends in organelle transport. *Journal of Cell Biology*, 158(2):305–319, 2002. ISSN 15408140. doi: 10.1083/jcb.200201029.
19. Armen J. Moughamian, Gregory E. Osborn, Jacob E. Lazarus, Sandra Maday, and Erika L.F. Holzbaur. Ordered recruitment of Dynactin to the microtubule plus-end is required for efficient initiation of retrograde axonal transport. *Journal of Neuroscience*, 33 (32):13190–13203, 2013. ISSN 02706474. doi: 10.1523/JNEUROSCI.0935-13.2013.
20. Hwajin Kim, Shuo-Chien Ling, Gregory C. Rogers, Comert Kural, Paul R. Selvin, Stephen L. Rogers, and Vladimir I. Gelfand. Microtubule binding by dynactin is required for microtubule organization but not cargo transport. *Journal of Cell Biology*, 176(5):641–651, feb 2007. ISSN 1540-8140. doi: 10.1083/jcb.200608128.
21. Nireekshit Addanki Tirumala and Vaishnavi Ananthanarayanan. Role of Dynactin in the Intracellular Localization and Activation of Cytoplasmic Dynein. *Biochemistry*, 59(2):156–162, 2020. ISSN 15204995. doi: 10.1021/acs.biochem.9b00772.
22. Nils Gustafsson, Siân Culley, George Ashdown, Dylan M. Owen, Pedro Matos Pereira, and Ricardo Henriques. Fast live-cell conventional fluorophore nanoscopy with ImageJ through super-resolution radial fluctuations. *Nature Communications*, 7, 2016. ISSN 20411723. doi: 10.1038/ncomms12471.
23. Takuya Kobayashi and Takashi Murayama. Cell Cycle-Dependent Microtubule-Based Dynamic Transport of Cytoplasmic Dynein in Mammalian Cells. *PLoS ONE*, 4(11):e7827, nov 2009. ISSN 1932-6203. doi: 10.1371/journal.pone.0007827.
24. Ewa Bielska, Martin Schuster, Yvonne Roger, Adokiye Berepiki, Darren M. Soanes, Nicholas J. Talbot, and Gero Steinberg. Hook is an adapter that coordinates kinesin-3 and dynein cargo attachment on early endosomes. *Journal of Cell Biology*, 204(6):989–1007, mar 2014. ISSN 1540-8140. doi: 10.1083/jcb.201309022.
25. Theodoros Matanis, Anna Akhmanova, Phebe Wulf, Elaine Del Nery, Thomas Weide, Tatiana Stepanova, Niels Galjart, Frank Grosveld, Bruno Goud, Chris I. De Zeeuw, Angelika Barnekow, and Casper C. Hoogenraad. Bicaudal-D regulates COPI-independent Golgi–ER transport by recruiting the dynein–dynactin motor complex. *Nature Cell Biology*, 4(12):986–992, dec 2002. ISSN 1465-7392. doi: 10.1038/ncb891.

26. Erik Nielsen, Fedor Severin, Jonathan M. Backer, Anthony A. Hyman, and Marino Zerial. Rab5 regulates motility of early endosomes on microtubules. *Nature Cell Biology*, 1(6): 376–382, oct 1999. ISSN 1465-7392. doi: 10.1038/14075.
27. D. M. Gowers, G. G. Wilson, and S. E. Halford. From The Cover: Measurement of the contributions of 1D and 3D pathways to the translocation of a protein along DNA. *Proceedings of the National Academy of Sciences*, 102(44):15883–15888, nov 2005. ISSN 0027-8424. doi: 10.1073/pnas.0505378102.
28. P. Hammar, P. Leroy, A. Mahmutovic, E. G. Marklund, O. G. Berg, and J. Elf. The lac Repressor Displays Facilitated Diffusion in Living Cells. *Science*, 336(6088):1595–1598, jun 2012. ISSN 0036-8075. doi: 10.1126/science.1221648.
29. Arthur D Edelstein, Mark A Tsuchida, Nenad Amodaj, Henry Pinkard, Ronald D Vale, and Nico Stuurman. Advanced methods of microscope control using Î¼Manager software. *Journal of Biological Methods*, 1(2):e10, nov 2014. ISSN 2326-9901. doi: 10.14440/jbm.2014.36.
30. Alexander Krull, André Steinborn, Vaishnavi Ananthanarayanan, Damien Ramunno-Johnson, Uwe Petersohn, and Iva M. Tolić-Nørrelykke. A divide and conquer strategy for the maximum likelihood localization of low intensity objects. *Optics Express*, 22(1):210, jan 2014. ISSN 1094-4087. doi: 10.1364/OE.22.000210.
31. Johannes Schindelin, Ignacio Arganda-Carreras, Erwin Frise, Verena Kaynig, Mark Longair, Tobias Pietzsch, Stephan Preibisch, Curtis Rueden, Stephan Saalfeld, Benjamin Schmid, Jean-Yves Tinevez, Daniel James White, Volker Hartenstein, Kevin Eliceiri, Pavel Tomancak, and Albert Cardona. Fiji: an open-source platform for biological-image analysis. *Nature Methods*, 9(7):676–682, jul 2012. ISSN 1548-7091. doi: 10.1038/nmeth.2019.